

Cherenkov τ Shower Earth-Skimming Method for PeV-EeV ν_τ Observation with Ashra

Y. Asaoka^a, M. Sasaki^a

^a*Institute for Cosmic Ray Research, University of Tokyo,
Kashiwa, Chiba 277-8582, Japan*

Abstract

We describe a method of observation for PeV–EeV tau neutrinos using Cherenkov light from the air showers of decayed taus produced by tau neutrino interactions in the Earth. Aiming for the realization of neutrino astronomy utilizing the Earth-skimming tau neutrino detection technique, highly precise determination of arrival direction is key due to the following issues: (1) Clear identification of neutrinos by identifying those vertices originating within the Earth’s surface; (2) Identification of very high energy neutrino sources. The Ashra detector uses newly developed light collectors which realize both a 42 degree-diameter field-of-view and arcminute resolution. Therefore, it has superior angular resolution for imaging Cherenkov air showers. In this paper, we estimate the sensitivity of and cosmic-ray background resulting from application of the Ashra-1 Cherenkov tau shower observation method. Both data from a commissioning run and a long-term observation (with fully equipped trigger system and one light collector) are presented. Our estimates are based on a detailed Monte Carlo simulation which describes all relevant shower processes from neutrino interaction to Cherenkov photon detection produced by tau air showers. In addition, the potential to determine the arrival direction of Cherenkov showers is evaluated by using the maximum likelihood method. We conclude that the Ashra-1 detector is a unique probe into detection of very high energy neutrinos and their accelerators.

Keywords: high-energy neutrinos, Earth-skimming tau neutrino, Cherenkov images, Ashra, CORSIKA, GEANT4, Monte Carlo simulation

1. Introduction

Gamma-ray bursts (GRBs), important high energy transient phenomena, are plausible candidates for cosmic ray sources up to and including the highest energy regions [1, 2, 3]. Following the identification of GRB970228 with arcminute resolution by Beppo-Sax satellite [4], understanding of GRBs progressed dramatically, owing to the collaboration of satellite-supplied GRB triggers and follow up multi-wavelength observations. As a result, the GRB standard model based on the particle acceleration in the internal/external shocks was established [5, 6, 7, 8]. On the other hand, observations of GRB and its afterglow made by Swift [9] and Fermi [10] satellites revealed various phenomena which are difficult to explain in the framework of the standard model. To resolve the various complicated aspects of the GRB physics mechanism, we would need “multi-particle astronomy” [11, 12] which uses other particles in addition to photons. In particular, neutrinos are the most important because with them it is possible to probe the optically thick region for electromagnetic components. As we can learn from Beppo-Sax’s success, identifying the source with superior angular resolution enables us to approach the physics mechanism by combining a number of observational results. To realize “multi-particle astronomy”, arcminute resolution would be desirable in the field of very high energy (VHE) neutrino observation.

The All-sky Survey High Resolution Air-shower detector (Ashra) is a project which primarily aims to observe Cherenkov and fluorescence lights from the lateral and longitudinal developments of very-high-energy (VHE) cosmic-ray air showers in the atmosphere. It uses newly developed light collectors (LCs) which realize both a 42 degree-diameter field-of-view (FOV) and arcminute resolution. In particular, it can capture air-shower images with unprecedented precision. It is expected to determine the arrival direction of parent particle with high accuracy.

As to detection methods for VHE neutrinos, there are methods which use water and/or ice as the neutrino target [13, 14], and those which utilize air showers, i.e., the deeply penetrating neutrino air-shower detection technique and recently proposed “Earth skimming tau-neutrino (ν_τ) technique” [15, 16, 17, 18, 19]. Some results have already been published with the Earth-skimming method (for example, see [20]). On the other hand, by combining Cherenkov emission in the optical band and “Earth skimming ν_τ technique” (Cherenkov tau shower Earth-skimming method; hereafter referred to as Cherenkov τ shower ES method), we can effectively survey an energy range which is hard to reach with the above mentioned technique. It is possible to achieve a maximum of sensitivity around 10–100 PeV in which the VHE neutrino signals from GRBs are expected. Figure 1 shows the expected neutrino fluence from nearby GRB, in which the calculated fluence from GRB030329 shown in Ref. [21] is scaled to different redshifts(z). The expected sensitivities of the Ashra-1 detector by using Cherenkov τ shower ES method are also plotted in the figure, where occurrence of GRB behind the mountain is assumed. The sensitivity calculation is performed by using the

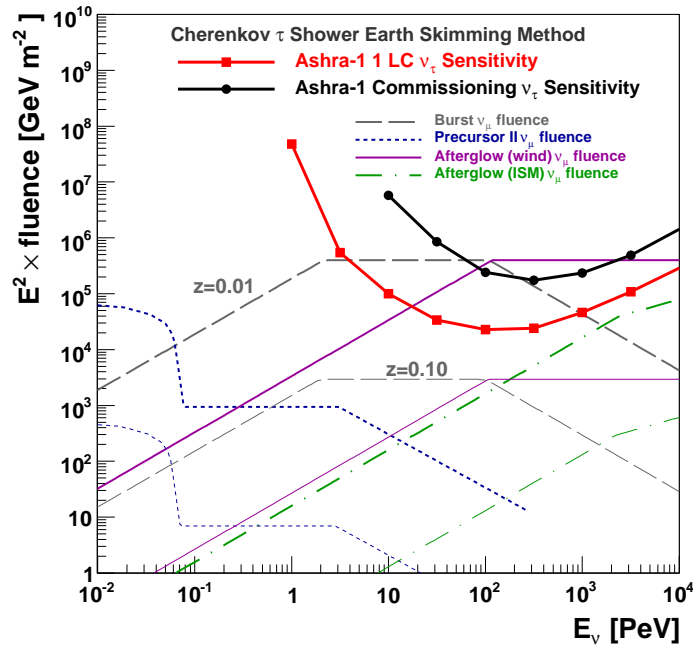


Figure 1: The sensitivity of Cherenkov τ shower ES method with Ashra-1 where occurrence of GRB behind the mountain is assumed (see the text). Solid square shows the differential sensitivity of the Ashra-1 observation using one light collector and solid circle shows that of the commissioning observation. Note that differential sensitivity represents the fluence where 2.3 events are expected at the corresponding energy decade. Also shown are the scaled neutrino fluence expected from GRB030329 occurred at $z = 0.01$ and $z = 0.1$ in each phase of GRB [21]. The nearest and second nearest GRBs to date were occurred at $z=0.0085$ (GRB980415 [22]) and $z=0.0331$ (GRB060218 [23]), respectively. The dashed, dotted, solid and dash-dotted lines show the components of burst, precursor, afterglow in wind environment, and afterglow in ISM environment, respectively.

Monte Carlo simulation described in detail in this paper.

This paper is organized as follows: Section 2 introduces the Ashra-1 detector, Section 3 describes the detailed method to simulate Earth-skimming ν_τ events, including the discussion about the deflection during their propagation. Section 4 shows the result of a sensitivity estimation. Section 5 discusses the systematic errors due to the incorporated Monte Carlo simulation, background estimation and angular reconstruction accuracy of τ shower events. We conclude in Section 6.

2. Ashra-1 Detector

The All-sky Survey High Resolution Air-shower detector Phase I (Ashra-1) is an optical-telescope based detector system [24] optimized to detect VHE particles. Ashra-1 is distinguished by two features: (1) an ultra wide optical system in which 42-degree FOV is demagnified to 1 inch by using photon and electron optics [25]; (2) the high resolution imaging system with trigger. Ashra-1 combines these unique features, resulting in very cost-effective pixels compared to conventional photomultiplier arrays at the focal surface of an optical telescope. Ashra-1 can observe the whole sky with arcminute resolution with 12 detector units pointing at different directions, where a detector unit consists of a few LCs pointing at the same direction.

The Ashra-1 detector system is designed so that the focal image is split into trigger/image capture devices after amplification. This feature enables us to simultaneously obtain 3 kind of phenomena which have different time scales, i.e., Cherenkov emission (ns), fluorescence (μ s), and starlight (s) without sacrificing the signal to noise ratio. By fully utilizing these distinct features, Ashra is aiming to undertake the full-fledged astronomical observation using VHE particles and trying to achieve the detection of VHE neutrinos for the first time using the Earth and the nearby mountain as the target [26], an arrangement provided by the Ashra-1 observatory being located on the Mauna Loa (3,300m) on Hawaii Island, opposite to the Mauna Kea. It can also be used to optically observe transient objects like GRBs as it monitors the whole sky simultaneously [27, 28].

3. Earth Skimming Tau Neutrino

3.1. Neutrino detection method

To detect VHE neutrinos, a large target volume is required in order to compensate for the very small neutrino-nucleon cross section. On that basis, the secondary particles produced by the first neutrino interaction are required to be detected through some method. The detection method using water and ice as a target detects Cherenkov light from secondary muons taking advantage of the fact that ice and water are to some extent optically transparent. This method can be categorized by identical target and detection volume. On the other hand, the detection method using deeply penetrating air showers from higher-energy neutrinos uses atmosphere as a target and detection volume. This method enables achieving a huge detection volume as the atmosphere has very high transmittance. However, it is difficult to obtain a larger target mass due to low atmospheric density. The detection method called Earth-skimming ν_τ technique [15, 16, 17, 18, 19] can realize a huge target mass and detection volume at the same time by separating the target and detection volume utilizing the interaction process of ν_τ . The detection method is described as follows (See Fig. 2): a VHE ν_τ interacts in the Earth or mountain and produces a tau lepton (τ). τ penetrates the Earth and/or mountain and enters in the atmosphere. Subsequently, it decays and produces an air shower. Cherenkov photons from the air shower are detected. Owing to the separation of the first interaction where ν_τ produces τ and τ decay generating air shower, air shower observation becomes possible while preserving the huge target mass required to compensate for the low cross section of the first interaction. For this detection method, it is crucial for the τ to go through the Earth and/or mountain before its decay, and to develop the air-showers in the atmosphere in front of the detector after its decay. Note that the decay length of 100 PeV τ is 4.9km. Here, “Cherenkov τ shower ES method” is defined as the detection method which detects Cherenkov photons from τ shower appearing from the Earth or the mountain fully utilizing this feature. Mauna Kea is over 3,200 km³ in volume and 9.3 tera tons in mass [29], making it the perfect location to implement an experiment using this technique.

3.2. Deflection from parent tau neutrinos

This section describes deflection of Cherenkov τ shower compared to the arrival direction of parent ν_τ in order to estimate the ability to trace back the direction of the detected air shower to the accelerator. We evaluated the deflection of the propagating particle in each step from the neutrino charged current interaction to τ propagation in the Earth, tau decay, and production of the extensive air shower. We used PYTHIA (ver. 6.1) [30] to evaluate the neutrino charged current interaction. Since $P_t < M_W$ (where M_W denotes the mass of the W boson which mediates the charged current interaction) and P_t denotes the transverse momentum of the produced τ , the deflection angle of τ ($\Delta\theta_\tau$) with respect to the parent ν_τ should be less than 0.3 arcmin for $E_\tau > 1$ PeV. The simulation results with PYTHIA were consistent with this.

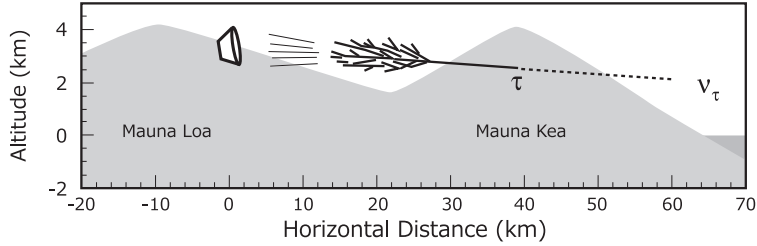


Figure 2: Schematic view of Cherenkov τ shower ES method. Mauna Kea is used as the target mass for neutrino charged current interaction. The produced air shower is observed from Mauna Loa. In addition to the fact that the mountain can be viewed with large solid angle from the observatory, the distance of about 30km from the observatory to the Mauna Kea surface is appropriate for the air shower development in 10–100 PeV energy range, resulting in the huge advantage of the Ashra-1 observatory.

Second, we used GEANT4 (ver. 9.3) [31] to evaluate the τ 's deflection due to propagation in the Earth. To estimate the energy loss of high energy leptons, the following parametrization is generally adopted [32]:

$$-\left\langle \frac{dE}{dX} \right\rangle = \alpha + \beta E,$$

where α denotes the nearly constant parameter determined by ionization loss, and β denotes the radiative energy loss due to Bremsstrahlung, pair production and photonuclear interaction. Since radiative energy loss is dominant for high energy τ s, these high energy process must be included in the "Physics List" of GEANT4. Thus, we applied the following processes originally defined for muons to τ s, and estimated the deflection after propagating through 10km rock.

- G4MuBremsstrahlung: Bremsstrahlung
- G4MuPairProduction: e^+e^- pair production ¹
- G4MuNuclearInteraction: Photonuclear Interaction

To validate our GEANT4 simulation, we compared the energy dependence of β for Bremsstrahlung, pair production, and photonuclear interaction to Ref. [32]. The β energy dependence agreed well for the former two processes, but we found that GEANT4 produced smaller values for photonuclear interaction at higher energy and that the difference was 3 times at 10^8 GeV. Therefore we wrote a toy Monte Carlo simulation for photonuclear interaction using the formalism of Refs. [33, 34]. In this simulation, the energy dependence of β in the relevant energy range was well reproduced within $\pm 1\%$ although the absolute value of β was 30% higher than that in the original work. Note that our estimate on τ 's deflection due to photonuclear interaction can be assumed to be conservative since larger deflection is expected from higher β . Figure 3 shows the simulation results of deflection angle of τ s after propagating 10km of rock. Left panel shows the GEANT4 results including all the high energy processes except for photonuclear interaction, and the right panel shows the results of photonuclear interaction simulated by our toy Monte Carlo simulation. These results indicate that photonuclear interaction becomes dominant for deflection at 1 PeV and higher. Note that the decay of τ s was switched off for above simulations and the hatched histograms indicate that the τ range is less than 10km. For example, the τ range is 4.9 km at 100 PeV. We conclude that the deflection angle of τ s with energy greater than 1 PeV is much less than 1 arcmin.

Next, the deflection due to τ decay is estimated by using the output of TAUOLA[35] taking the τ polarization into account. From the mass of the τ s, the deflection angle must be less than 1 arcmin if the energy of the secondary particle is higher than 13 TeV. Using TAUOLA outputs in our simulation sample of PeV-energy neutrinos, we found that the probabilities to produce decay particle with its energy less than 13 TeV were 1.7% and 0.038% for parent

¹we modified the original G4MuPairProduction so that the momentum preserves including the produced particles, resulting in the inclusion of deflection.

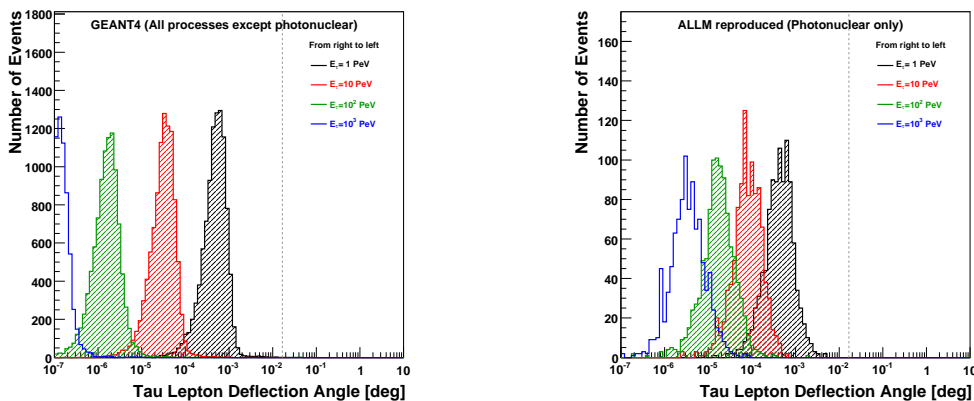


Figure 3: The simulation results of deflection angle of τ s after propagating 10km of rock. (*Left*) the GEANT4 results including all the high energy processes except for photonuclear interaction. (*Right*) the results of photonuclear interaction simulated by handmade simulation. Note that the decay of τ s was switched off for the above simulations. The hatched histograms indicate that the τ range is less than 10km.

neutrino energies of 1 PeV and 10 PeV, respectively. Furthermore, none of the simulated events with $E_\tau > 13.7$ TeV satisfied the trigger requirements in both of Commissioning and Ashra-1 detector configurations. We conclude that the deflection angle between decay particles which produce the air shower and parent ν_τ was less than 1 arcmin for detectable events.

Finally, the direction of the hadron air shower was evaluated using CORSIKA (ver. 6.900). At the shower maximum, we compared the direction of the parent particle (charged pion) to that of electrons and positrons which are the dominant producers of Cherenkov photons. We found that on average the direction of electrons and positrons and the parent particle of the air shower was coincident within 0.1° at 1 PeV. In conclusion, we found that the arrival direction of PeV ν_τ s was preserved within 0.1° including the hadron air-shower generation. The accurate reconstruction of the arrival direction by means of fine imaging will be a very powerful technique to determine point sources of PeV ν_τ s.

3.3. Monte Carlo simulation

To investigate the neutrino identification capability and sensitivity, it is vital to develop a detailed Monte Carlo simulation which simulates all processes from the neutrino interaction to detection of Cherenkov photons produced by decayed τ air showers. An earlier study mainly based on an analytic approach can be found in Ref.[36]. In our simulation, the first step is to generate the ν_τ s from the certain area and solid angle which is large enough compared with our detector's detection volume. In this step, τ production due to the charged current interaction of ν_τ , τ propagation in the Earth, and the determination of the decay point of τ s emerging from the Earth are simulated. These processes calculate the τ flux emerging from the Earth and subsequent decay in the atmosphere. The flux is calculated for ν_τ s whose energies range from 10^{15} eV (1 PeV) to 10^{20} eV (100 EeV) in steps of 0.5 decades. The simulation code used in this step is based on the Earth skimming ν_τ simulation code described in Ref.[37]. The code is further developed to include the mountain skimming effect. Neutrino and τ interactions are updated from Ref.[37] in part in a relation with the previous work described in Ref.[38] and are described in the following. The code is hereafter denoted as TauSim. Considering the direction and energy of τ s emerging from the Earth and removing the events with no probability of detection at this step, the efficiency of the simulation was substantially improved.

For the neutrino-nucleon cross section, we used the calculation [39] based on CTEQ4-DIS parton distribution functions (PDFs). Inelasticity is considered by fitting its energy dependence shown in Ref. [40] to a quadratic expression. To estimate the energy losses due to propagation of τ s in the Earth, we used the parametrization shown in Ref. [41] based on Ref. [32]. As the density of the Earth's crust, we took 2.9 g/cm^3 [42] since the main component of the Earth's crust around Hawaii is basalt.

The second step of our simulation deals with τ decay, air-shower generation, and detection in the detector. Four vectors of secondary particles produced by τ decay were calculated by TAUOLA version 2.4 [35]. The polarity

of τ was set to -1 [37]. The decay mode was determined for each τ obtained in the first step, resulting in 1–4 secondary particle(s). Then, an air shower was generated taking into account the geometrical relationship between the air shower and the detector. We used CORSIKA [43] to simulate the air showers. Since high energy air-shower generation requires a large amount of CPU power, we used a thinning algorithm. To keep the fineness of the shower image taken by the detector as much as possible, we adopted a smaller value of thinning level = 10^{-7} . We used QGSJET [44] as high-energy hadron interaction model. In CORSIKA, incoming photons to the detector’s FOV were recorded by using the IACT package², and used in the detector simulation. The detector simulation incorporated the light collection area obtained by ray tracing of the optical system, measured transmittance, and quantum efficiency of photoelectric lens image intensifier tube [25]. The detailed calibration method and final validation using cosmic ray observation in commissioning phase is described in Ref.[26]. Trigger decision and acquisition of fine images were carried out in this step. Since CORSIKA output includes the generation height and wavelength of detected Cherenkov photons, attenuation in the atmosphere was considered here.

Figure 4 shows an example of neutrino shower events simulated for the detector configuration of commissioning observation obtained by the Monte Carlo simulation described above. The origin of horizontal and vertical axis in Fig.4 is set to the center of the light collector’s FOV, which is located at an altitude of 11.7° and an azimuthal angle of 22.1° . The unique capabilities of the Ashra detector enable us to obtain unmatched detailed images of Cherenkov showers. In the commissioning observation, we used a limited 62 channels of photo multipliers as trigger sensors to cover the view of the surface area of Mauna Kea as much as possible to maximize the sensitivity [26]. Adjacent-two logic was applied to trigger the fine imaging to reduce the background events due to the fluctuation of night sky background. In the Ashra-1 observation with final configuration, the trigger pixel size will be halved (to one quarter of the current pixel area) and the entire FOV of the LC will be covered by the trigger sensor.

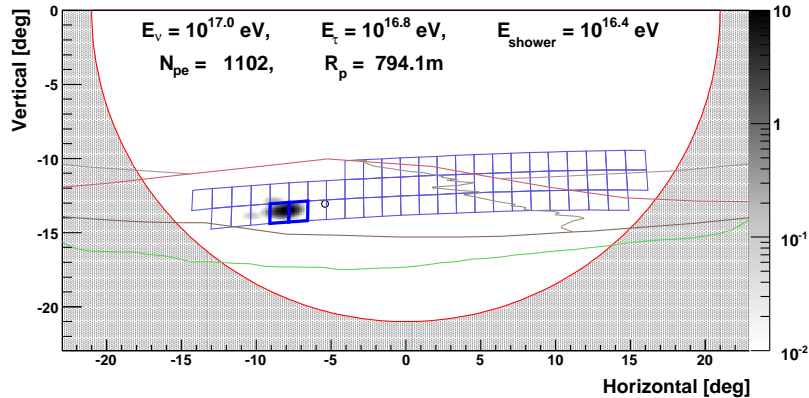


Figure 4: An example of the neutrino shower image obtained by the detailed Monte Carlo simulation with the configuration of commissioning observation. The origin of horizontal and vertical axis is set to the center of the light collector’s FOV, which is located at an altitude of 11.7° and an azimuthal angle of 22.1° . Boundary (large red circle) between the inside (open circle) and outside (hatched area) of the FOV of the Ashra-1 light collector, which faces Mauna Kea, and the layout of trigger pixel FOVs (blue boxes, firing trigger pixels with thick blue boxes) for commissioning observation are shown. The ridge lines of Mauna Kea (red) and Mauna Loa (green) mountains, the horizon, and Mauna Kea access road are also shown (gray). Open circle corresponds to the assumed typical point source coordinate with altitude -1.7° and azimuthal angle 16.2° .

4. Sensitivity

The effective area (A_{eff}) is calculated for each ν_τ energy (E_{ν_τ}) ranging from 1 PeV to 100 EeV in steps of 0.5 decades. At first, from the direction of the point source, N_{total} ν_τ events are uniformly generated in the large area

²Since the IACT package in CORSIKA ver. 6.900 cannot receive the thinning information correctly, we fixed it to use in our simulation.

(A_{eff}^0) containing Mauna Kea. Assuming that N_{det} are finally triggered and detected from N_{total} events, the following equation gives $A_{\text{eff}}(E_{\nu_\tau})$ as a function of neutrino energy.

$$A_{\text{eff}}(E_{\nu_\tau}) = A_{\text{eff}}^0 \frac{N_{\text{det}}(E_{\nu_\tau})}{N_{\text{total}}(E_{\nu_\tau})}.$$

The left panel of Figure 5 shows an overlay of the effective area of 1-LC observation with final configuration and of the commissioning observation assuming typical point source coordinates with altitude -1.0° and azimuthal angle 17.1° , which is indicated as the open circle in Fig.4. The commissioning observation used the measured trigger threshold described in Ref.[26], and 1-LC observation used the trigger threshold of 20 photoelectrons per pixel which corresponds to $\sim 1/7$ of that in the commissioning observation. In both cases adjacent-2 trigger logic was used. The same neutrino shower samples were used to estimate the sensitivities for the detector configuration of commissioning and 1-LC observations although trigger simulations were carried out separately. The right panel of Figure 5 shows the effective aperture for a diffuse neutrino source where the neutrino direction and incident position are uniformly scanned. In both cases of point and diffuse sources, improved sensitivity of 1-LC observation was achieved due to halved trigger pixel size, full coverage of light collector's FOV by trigger pixels, and lower trigger threshold. Although there is no additional cut applied to estimate the effective area and effective aperture other than trigger decision, the triggered signal tends to have a much larger number of photoelectrons than the minimum number required for a triggerable signal even in the 1-LC configuration. For example, the sensitivity weighted average of photoelectrons for triggered events in the 1-LC configuration was estimated to be ~ 1000 for neutrino shower samples generated to estimate the diffuse neutrino aperture. Note that the sensitivity weight for each neutrino energy was calculated assuming a typical E_ν^{-2} flux. In the resultant photoelectron distribution, $\sim 2\%$ of events have less than 100 photoelectrons. The bunch size distribution of the generated showers in the CORSIKA output was also studied and it was found that 99% of them had 20 bunches or more (at least 10 times of trigger pixels to be fired) when detected number of photoelectrons was 40 or more, resulting in the validation of the applied thinning level of 10^{-7} in terms of sensitivity estimation.

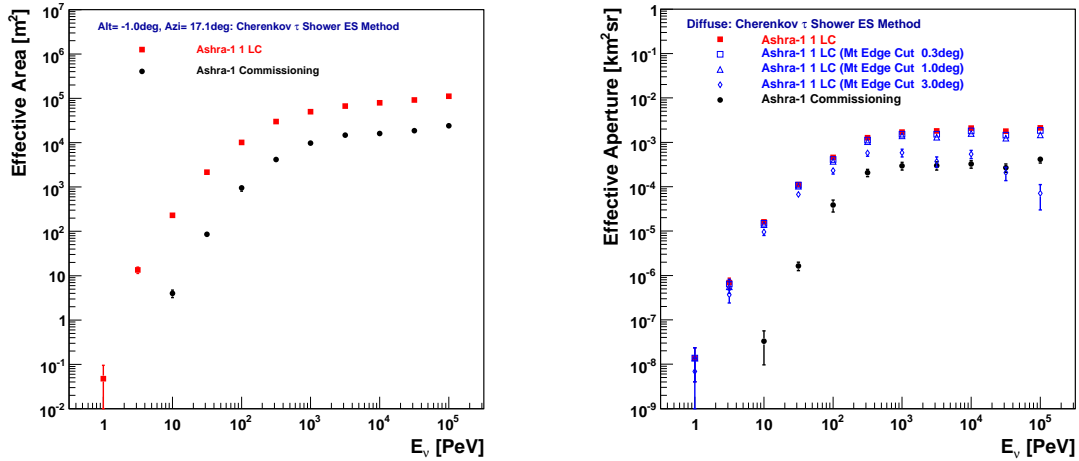


Figure 5: Typical effective area (*Left*) and effective aperture (*Right*) of Cherenkov τ shower ES method with Ashra-1. The effective area was estimated in the case of an altitude of -1.0° and an azimuthal angle of 17.1° as an arrival direction of ν_τ s. Red solid squares and black solid circles represent the sensitivity of 1 light-collector observation and the commissioning observation, respectively. Blue open squares, blue open triangles, and blue open diamonds represent the effects of mountain-edge cut of 0.3° , 1.0° , and 3.0° , respectively. For explanation of mountain-edge cut, see the text.

5. Discussion

5.1. Systematic errors

The dominant systematic errors associated with the sensitivity of Cherenkov τ shower ES method can be summarized as follows:

- neutrino-nucleon interaction cross section;
- τ propagation in the Earth;
- density of the Earth's crust and the geodetic model.

In the following, the systematic uncertainties which worsen the resultant 90% upper limit on ν_τ fluence and/or flux are considered.

At first, the systematic uncertainty of the neutrino-nucleon interaction cross section was addressed. As explained, we used the calculation based on CTEQ4 [39] for the total cross section of the neutrino-nucleon interaction. However, there is a large model uncertainty at higher energies due to inconsistency between PDF sets [45, 46, 47, 48, 49]. Among these models, Refs. [45, 48] are based on the next-to-leading order linear dynamics [Dokshitzer-Gribov-Lipatov-Altarelli-Parisi (DGLAP)] constrained by HERA data. The Auger experiment quoted a systematic uncertainty of +5%–9% for the expected neutrino rate [50] due to cross section uncertainty based on Ref. [48]. To include non-linear effects which become important at smaller Bjorken x , Ref. [46] uses unified DGLAP/Balitsky-Fadin-Kuraev-Lipatov (BFKL) evolution supplemented by screening effects as well as nuclear shadowing. Ref. [47] uses color glass condensate (CGC) formalism which fits data from RHIC. We took calculations based on a dipole model [51] as the representative of CGC models, since they have the advantage that the BFKL anomalous dimension is built in [47], and since the other models based on a different dipole model [52] require a big assumption to determine the gluon distribution function at smaller Bjorken x [47]. Ref. [49] considers the imposition of Froissart unitarity not to violate the Froissart bound at higher energy. From the largest difference between these models and the CTEQ4 parameterization in the relevant energy range, the systematic error of the neutrino-nucleon interaction cross section was estimated to be –35%.

Next, we evaluated the systematic errors of τ propagation in the Earth. We used the approach from Refs.[32, 53] to calculate the energy loss by the τ during propagation through the Earth and the mountain at PeV energies. The uncertainty due to the structure function used in the energy loss calculation defined as the discrepancy between predictions of the energy loss of the τ at 10 PeV by different theoretical models was found to be +50% [53].

Finally, as we did not use typical values for the Earth's crust, we considered the uncertainty in crust density itself. Because the incident direction of ν_τ events in the effective FOV is almost horizontal, we adopted the constant value of 2.9 g/cm^3 [54] which is the density of basalt, the dominant component in the surface layer of the Earth's crust in the vicinity of Big Island of Hawaii. We took –10% as a conservative systematic uncertainty on the density, which is the difference between the average density of Earth's crust (2.6 g/cm^3)[42] and the density of basalt.

In Ref.[26], we evaluated the systematic uncertainty for the resultant upper limit by conservatively assuming a linear or reciprocal relationship with the uncertainties when we considered the involved physical processes. In this paper, to evaluate the relation between each source of systematic errors and the resultant upper limit in detail, we performed a number of simple Monte Carlo simulations using TauSim with different parameter sets. The lower cut on the shower energy to simulate the trigger decision in the simplified simulation was estimated using full Monte Carlo simulation results obtained with CORSIKA. Using the estimated energy cut, the energy dependent apertures and effective areas for 1-LC and commissioning observation match the full simulation within 13% and 16% precision, respectively. Effects on fluence/flux limit were evaluated assuming a typical E^{-2} tau neutrino flux. The obtained systematic errors for the resultant upper limit are summarized in Table 1, where the column labeled "Estimation method" represents the uncertainty due to using the simple Monte Carlo simulations described above, and thus the factors of 1.13 and 1.16 should be multiplied to the other error sources.

As to the geodetic model, we used detailed topographical data of the area around Mauna Kea and our own measurements of the mountain shape from the Ashra site to evaluate the effects on the resultant limit. Although a simple 5-sided pyramid was defined in TauSim to calculate tau lepton fluxes emerging from the mountain, the residuals from using the detailed topography were checked and the effect on the limit was estimated by considering a smaller and a

Syst. Error Source	Source Error	1-LC (diffuse)	Commissioning (GRB081203A)
ν Cross Section	-35%	32%	37%
τ Energy Loss	+50%	14%	14%
Rock Density	-10%	5%	4%
Geodetic Model	—	13%	2%
Estimation Method	—	13%	16%

Table 1: Summary table of systematic errors for the resultant upper limit. The column labeled "Estimation method" represents the uncertainty due to the simpler limit calculation method which omit the CORSIKA shower generation and the detailed trigger decision.

larger 5-sided pyramid, covering the mountain shape by 84% and being 84% covered by it, respectively. It is negligible for observation of GRB081203A in the commissioning observation described in Ref.[26]. In 1-LC observation, the effect is slightly larger and was estimated to be 13% for the limit on diffuse neutrino flux. The effects caused by the different density of the ocean compared to rock were also included in the study.

Deviation from the linear relation in the propagation of the cross-section systematic error is due to the shielding of tau neutrinos by the Earth. We confirmed that the smaller cross section results in higher sensitivity in the higher energy region at lower elevation where the chord length of skimmed Earth is long enough to start shielding incoming neutrinos. Only a weak relation between tau energy losses in the rock and the sensitivity was observed at lower energy due to the τ s predominantly decaying before any significant energy loss. Tau energy losses become more and more important at higher energies, and thus lower energy loss results in higher sensitivity. However, this relation reverses at $E_\nu \geq 1$ EeV where the chord length is short enough for not the whole τ energy being absorbed, because τ s of lower energy appearing from the Earth have a higher probability to decay in front of the light collector. In this situation, higher energy loss results in higher sensitivity. Due to the combination of these facts, the systematic uncertainty in τ energy losses is not a major factor in the sensitivity estimation. Although uncertainty on the rock density affects both the neutrino interaction and τ energy losses, the resultant uncertainty on the sensitivity is small because the effects basically cancel each other out.

5.2. Angular resolution

As discussed in Section 3.2, Cherenkov τ shower of $E > 1$ PeV preserves the arrival direction of the parent ν_τ to within 0.1° accuracy. This means that the detector's ability to reconstruct the arrival direction precisely results in the identification of the VHE neutrino sources and leads to the realization of "multi particle astronomy". Owing to its high-resolution imaging capability, the Ashra-1 detector has a huge potential to improve the reconstruction of the arrival direction of ν_τ induced air showers. In this section, shower reconstruction with likelihood analysis will be discussed, where simulated air-shower images are generated with faster Gaisser-Hillas and NKG parametrization [37], which are well established [55, 56].

In this study, we adopted the following geometrical event reconstruction parameters:

(n_x, n_y) : Shower axis direction in the obtained fine image;

(X', Y') : Intersection of mountain surface with the shower axis (tau emerging point) projected into the obtained fine image.

E : Shower energy.

(n_x, n_y) and (X', Y') determines the geometrical relationship between the detector and the shower axis, and therefore the impact parameter (R_p). Easy and direct comparison between real and simulated data was attained by adopting the positions in the obtained image as the parameters for event reconstruction. The positions in the obtained image correspond to the directions in the light collector's FOV. For investigation of the reconstruction capability, we simulated a 10 PeV proton shower incoming at a zenith angle of 65° . For this type of event, the definition of (X', Y') has to be different. We took the intersection of 25 km height with the shower axis projected into the obtained image as (X', Y') .

The following geometrical reconstruction parameters were taken as a typical shower example to study the reconstruction accuracy:

$$(n_x, n_y) = (0.0, 0.0) \text{ [deg];}$$

$$(X', Y') = (0.6, 0.0) \text{ [deg];}$$

$$E = 10 \text{ [PeV].}$$

This parameter set corresponds to $R_P = 540$ m. The left panel of Figure 6 contains an example of the shower image generated with this parameter set, and it serves as a "dummy real data" to study reconstruction accuracy. The right panel of Figure 6 shows the probability density distribution obtained by averaging 10^6 events generated with the same parameter set. To generate the shower images, the longitudinal and lateral development of air shower was calculated using Gaisser-Hillas and NKG, respectively. The direction of Cherenkov photon was calculated by using the parametrization described in Ref. [57], where normalization was adjusted to reproduce the R_P dependence of the detected number of photoelectrons (N_{pe}) obtained with CORSIKA. We confirmed that the R_P dependence is reproduced within $\pm 15\%$ within the R_P range we used in this study. In this simulation, fluctuation due to the first interaction point was taken into account, but air-shower fluctuation due to hadron interaction was not. This effect was accounted for in Section 3.2 (0.1° at 1 PeV). Although it is preferable to include hadron air-shower fluctuation using CORSIKA, generating a sufficient number of events requires an amount of CPU power unavailable during the writing of this paper.

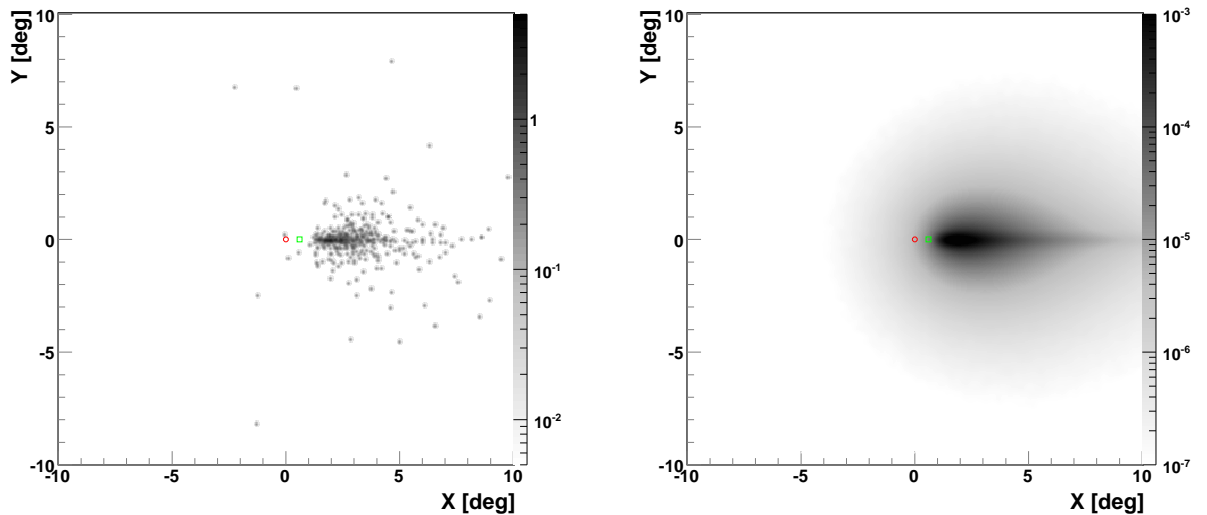


Figure 6: (Left) An example of Cherenkov shower image for event reconstruction ("dummy real data"), (Right) Probability density distribution. Red open circles represents (n_x, n_y) and green open square represents (X', Y') . Both images are obtained using the simulated air-showers generated using Gaisser-Hillas and NKG.

Using the number of photoelectrons in pixel i (N_{pe}^i) and the photon detection probability at the pixel (p_i), the log likelihood multiplied by -2 , which is compatible with chi-square, can be written as follows:

$$L = -2 \sum_i N_{pe}^i \log(p_i). \quad (1)$$

Note that the N_{pe}^i in each pixel was not discretized, as the photoelectric image pipeline distributes the corresponding charge because of its finite resolution. To estimate errors on the reconstruction parameters, it is necessary to calculate the error matrix for the likelihood function defined above. The error matrix is given as the inverse of the second order

partial differential matrix of the likelihood function as follows:

$$L = L(a_i^*, a_j^*) + \frac{1}{2}(a_i - a_i^*)^2 \frac{\partial^2 L}{\partial a_i^2} + \frac{1}{2}(a_j - a_j^*)^2 \frac{\partial^2 L}{\partial a_j^2} + (a_i - a_i^*)(a_j - a_j^*) \frac{\partial^2 L}{\partial a_i \partial a_j} \quad (2)$$

$$H_{ij} = 2M_{ij} = \frac{\partial^2 L}{\partial a_i \partial a_j} \quad (3)$$

$$R = M^{-1}, \quad (4)$$

where a_i represents the parameter and a_i^* represents the parameter value corresponding to the local minimum. R represents the error matrix, and M represents the second order partial differential matrix. M can be calculated by using the neighborhood values of L around the local minimum.

$$\frac{\partial^2 L}{\partial a_i \partial a_j} = \left(L - L(a_i^*, a_j^*) - \frac{1}{2}(a_i - a_i^*)^2 \frac{\partial^2 L}{\partial a_i^2} - \frac{1}{2}(a_j - a_j^*)^2 \frac{\partial^2 L}{\partial a_j^2} \right) \times \frac{1}{(a_i - a_i^*)(a_j - a_j^*)} \quad (5)$$

The inverse of M gives R and, once the error matrix is obtained, the diagonal elements correspond to the parameter errors including correlation between parameters. Elements of the correlation matrix are given by the following equation.

$$C_{ij} = \frac{R_{ij}}{\sqrt{R_{ii}R_{jj}}} \quad (6)$$

Using the "dummy real data" events generated by the Monte Carlo simulation, the correlation between reconstruction parameter was evaluated using the inverse matrix calculations described above. For simplicity, the energy of the shower was fixed for this calculation. The following example of an obtained correlation matrix shows that there are strong correlations between n_x and X' .

	n_x	n_y	X'	Y'
n_x	1.00	0.04	0.95	0.03
n_y	0.04	1.00	0.04	0.78
X'	0.95	0.04	1.00	0.02
Y'	0.03	0.78	0.02	1.00

Considering the fact that X' determines R_p , strong correlation between n_x and R_p results in a worse joint resolution. This is a well-known problem connected with the mono detection of Cherenkov shower and is greatly improved in case of stereo detection with multiple light collectors. In order to estimate the angular resolution of the reconstruction, therefore, we scanned n_x and X' space with 0.05° grid to search for the minimum of L while fixing n_y and Y' . To keep N_{pe} constant over different R_p data sets, the energy of the shower was adjusted. Since N_{pe} and R_p are inversely correlated, parameter sets with larger R_p are given larger shower energy. 200 events of "dummy real data" were generated using the same parameter set, but with different first interaction points and different random seeds. Since the maximum likelihood method uses the slope of probability density distribution, it is important to include the night sky background (NSB) photoelectrons. NSB photoelectrons were added as a probability per pixel in probability density distribution. To each dummy real data event, photonelectrons randomly distributed according to this probability were generated and added as well. We estimated the region for which the likelihood is calculated by using each "dummy real data" by defining cut positions which correspond to 5% of the peak in the projections of major and minor axes. In the major and minor axis projection, we used asymmetric and symmetric Gaussian to fit their shape, respectively, and calculated the 5%-peak positions to reduce the effects of statistical fluctuation toward the tails of the distributions.

After selecting (n_x, X') which gave minimum L in each "dummy real data", the distribution of residuals between the reconstructed and true directions (Δn_x ; defined as reconstructed minus true positions in the obtained image) was obtained. We found that the distribution has an offset toward positive side, meaning the smaller R_p , corresponding to smaller $X' - n_x$, tends to have minimum L . This was mainly due to the limited range of the likelihood calculation forced by the existence of NSB photoelectrons. In order to correct for this effect, application of a correction as a function of observable quantities was necessary. The observable quantities required for the correction are N_{pe} and an estimator

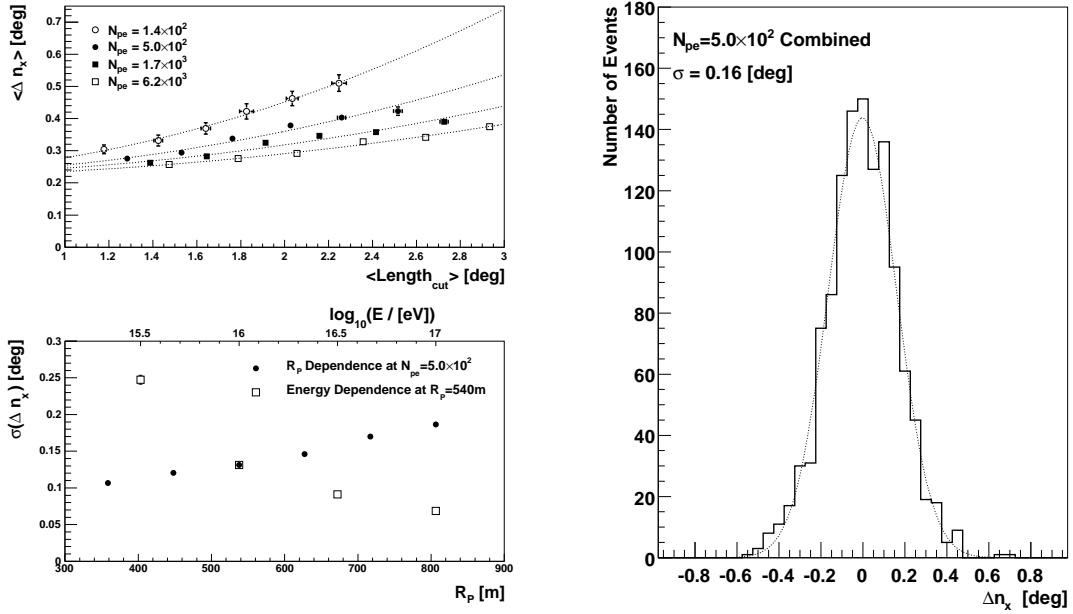


Figure 7: (Upper Left) The dotted curves represent correction function for Δn_x offset ($F_C(N_{\text{pe}}, \text{Length}_{\text{cut}})$). Open circles, closed circles, closed squares, and open squares represents the relation between $\langle \Delta n_x \rangle$ and $\langle \text{Length}_{\text{cut}} \rangle$ for $N_{\text{pe}} = 140, 500, 1700,$ and 6200 , respectively. (Bottom Left) The R_p dependence (closed circles) and energy dependence (open squares) of the angular resolution along the major axis ($\sigma(\Delta n_x)$). Energy dependence is shown at the fixed R_p of 540m while the R_p dependence is shown at fixed N_{pe} of 500. (Right) Residuals between the reconstructed and true directions (Δn_x) after correcting Δn_x offset. The distribution includes all the parameter sets of $(n_x, X') = (0.0, 0.4), (0.0, 0.5), (0.0, 0.6), (0.0, 0.7), (0.0, 0.8), (0.0, 0.9)$ [deg] for $N_{\text{pe}} = 500$ (see the text).

of R_p . We used $\text{Length}_{\text{cut}}$ as the estimator of R_p , where $\text{Length}_{\text{cut}}$ is defined as the 5%-peak cut length along the major axis. The upper left panel of Fig.7 shows the resultant correction function for Δn_x offset ($F_C(N_{\text{pe}}, \text{Length}_{\text{cut}})$) as dotted curves. Open circles, closed circles, closed squares, and open squares represents the relation between $\langle \Delta n_x \rangle$ and $\langle \text{Length}_{\text{cut}} \rangle$ for $N_{\text{pe}} = 140, 500, 1700,$ and 6200 , respectively, where $\langle \Delta n_x \rangle$ and $\langle \text{Length}_{\text{cut}} \rangle$ denotes the averaged value of Δn_x and $\text{Length}_{\text{cut}}$ for each parameter set, respectively. For each N_{pe} data set, X' was scanned from 0.4° to 0.9° in step of 0.1° , corresponding to the points from left to right. Each N_{pe} data set was used to obtain $F_C(N_{\text{pe}}, \text{Length}_{\text{cut}})$ with the fit to second order polynomial.

The R_p dependence on the angular resolution of n_x ($\sigma(\Delta n_x)$) is shown in the bottom left panel in Fig. 7 as closed circles, together with the energy dependence on $\sigma(\Delta n_x)$ as open squares, where $\sigma(\Delta n_x)$ corresponds to the root mean square of the Δn_x distribution. Energy dependence is shown at the fixed R_p of 540m while the R_p dependence is shown at fixed N_{pe} of 500. Slight worsening of the angular resolution is visible as R_p increases, where the data corresponds to $(n_x, X') = (0.0, 0.4), (0.0, 0.5), (0.0, 0.6), (0.0, 0.7), (0.0, 0.8), (0.0, 0.9)$, respectively, from left to right. On the other hand, clear worsening of the angular resolution proportional to square root of N_{pe} is observed in energy dependence, while a resolution better than 0.1° is obtained with sufficient N_{pe} at higher energies.

After applying the correction function in an event-by-event basis using the calculated $\text{Length}_{\text{cut}}$ and N_{pe} for each "dummy real data" sample, the Δn_x distribution from all parameter sets was obtained as shown in the right panel of Fig.7. The resultant angular resolution was estimated to be 0.16° . Considering the fact that N_{pe} for the parameter sets $N_{\text{pe}} = 500$ and the expected N_{pe} from tau neutrino signal as discussed in Section 4, the geometrical parameters used here would be appropriate to estimate the background contamination since they correspond to the events with less statistical power. This analysis outlined the fact that the high-resolution Cherenkov imaging would lead to the high accuracy reconstruction of the arrival direction, even with the mono detection of Cherenkov showers.

5.3. Background

In this section, we evaluate the background events due to air showers. Background events due to the detector itself are discussed in Ref. [26]. Air-shower background candidates are normal cosmic rays, muons, muon neutrinos, τ s, and ν_τ s. From simple flux calculations, it was shown that the neutrino components through mountain, prompt τ components and muons are negligible [38, 58, 59, 60, 61]. Thus, the large zenith angle component of normal cosmic rays was considered as the dominant background component in this study. To simulate this background, CORSIKA was used in the same way as with the ν_τ simulation. To consider the atmospheric depth correctly, "CURVED EARTH" option was selected. The IACT package was used to simulate incoming Cherenkov photons. Protons were selected as the parent particle and a thinning parameter of 10^{-5} was applied. To investigate the zenith angle and the energy dependence of the background flux, a difference in thinning level between this simulation and the ν_τ simulation was unavoidable. The bunch size distribution of the generated showers was studied in this case, too. We found that 74% (93%) of them had 20 (5) bunches or more when detected number of photoelectrons was 40 or more. The applied thinning level of 10^{-5} was acceptable in terms of background estimation precision.

At first, to estimate the background rate during the commissioning observation, the trigger rate for trigger-pixel arrangement adopted in the commissioning observation was calculated. As we could not simulate the largest zenith angle (θ_{zen}) of $\theta_{\text{zen}} > 88^\circ$ in the combination of "CURVED EARTH" and IACT options, trigger pixels were offset by two degrees toward higher elevation to estimate the trigger rate for $88^\circ < \theta_{\text{zen}} < 90^\circ$. To account for the trigger rate decrease due to thicker atmospheric depth, the result was further corrected by the ratio of expected events between $84^\circ < \theta_{\text{zen}} < 86^\circ$ and $86^\circ < \theta_{\text{zen}} < 88^\circ$ in the event that the entire FOV was covered by the trigger pixel. As a result, the number of expected background events (N_{CR}) due to normal cosmic rays during commissioning observation of 197.1 hr was estimated to be:

$$N_{\text{CR}} = 1.3 \times 10^{-4},$$

which is small enough to be neglected. Note that the above discussion did not use an event selection to discard cosmic rays using the reconstructed arrival direction information.

Next, the cosmic-ray background in 1-LC observation with final configuration was evaluated. With the maximum weather efficiency of 100%, 1750 hr of observation time is expected in one year. Assuming a trigger pixel threshold of 20 photoelectrons which is the same as for our sensitivity estimation, the cosmic-ray shower event rate emerging from the sky region near the mountain edge was found to be 8.2×10^{-2} , 0.55, 4.3, 39 (per year) within 0.1° , 0.3° , 1.0° , 3.0° from the mountain edge, respectively. Assuming perfect reconstruction of the arrival direction, a background-free result is achieved by requiring that the reconstructed direction of the shower axis points back toward the mountain or the Earth because they completely absorb any cosmic-ray secondary particles. In practice, the background-free result will be achieved by requiring a mountain-edge cut in which the reconstructed arrival direction is inside the mountain edge by θ_{cut} , where θ_{cut} is an angle dependent on the reconstruction accuracy. The resultant yearly background rate ($N_{\text{CR}}^{\text{1LC}}$) is calculated as follows:

$$\begin{aligned} N_{\text{CR}}^{\text{1LC}}(\theta_{\text{cut}}) &= \int_0^{\theta_{\text{max}}} n_{\text{CR}}(\theta) \int_0^\pi p_{\text{axis}}(\phi) \int_{-\infty}^{-(\theta+\theta_{\text{cut}})/|\sin\phi|} p_{\text{rec}}(\theta') d\theta' d\phi d\theta \\ &+ \int_0^{\theta_{\text{max}}} n_{\text{CR}}(\theta) \int_{-\pi}^0 p_{\text{axis}}(\phi) \int_{(\theta+\theta_{\text{cut}})/|\sin\phi|}^\infty p_{\text{rec}}(\theta') d\theta' d\phi d\theta \end{aligned} \quad (7)$$

where θ is defined as the vertical angle from the mountain edge (positive toward the sky region), θ_{max} represents the maximum angle from the mountain edge in the FOV, ϕ represents the angle between major axis of the shower image and the horizontal axis, $p_{\text{axis}}(\phi)$ denotes the probability to obtain the major axis at an angle ϕ , $p_{\text{rec}}(\theta)$ denotes the misreconstruction probability distribution to obtain the angular deviation from the true value by θ along the major axis, and $n_{\text{CR}}(\theta)$ denotes the background rate per radian. In this calculation, the deviation along the minor axis is neglected. An example of $p_{\text{rec}}(\theta)$ is shown in the right panel of Fig.7, where Δn_x corresponds to θ . $p_{\text{axis}}(\phi)$ is normalized as

$$\int_{-\pi}^\pi p_{\text{axis}}(\phi) d\phi = 1. \quad (8)$$

Using this notation, for example, the expected background rate emerging from the sky region within 1.0° from the

mountain edge can be expressed as follows:

$$\int_0^{1.0^\circ} n_{\text{CR}}(\theta)d\theta = 0.55. \quad (9)$$

θ_{cut} will be determined so that the resultant $N_{\text{CR}}^{\text{ILC}}(\theta_{\text{cut}})$ is small enough. Although it requires a more detailed procedure to apply this background rejection scheme for real data analysis, the discussion in this section and the previous section clearly illustrate its working principle.

It is important to evaluate the effective aperture dependence on the mountain-edge cut. By using the neutrino simulation data set, the effective aperture was estimated to be 90%, 80% and 38% of that without the cut for the mountain-edge cuts of 0.3° , 1.0° and 3.0° , respectively. The right panel of Figure 5 shows the energy dependence of effective apertures with the mountain-edge cuts by open symbols. Blue open squares, blue open triangles, and blue open diamonds represent the effects of the mountain-edge cuts of 0.3° , 1.0° , and 3.0° , respectively. The effective aperture with the 3.0° mountain-edge cut was shown to estimate the θ_{cut} dependence of the effective aperture although 3.0° is too large compared with the Ashra-1 angular resolution. The large decrease in the effective aperture at higher energy in the 3.0° mountain-edge cut is due to the fact that higher energy neutrinos could only be emerging from the mountain edge because of smaller interaction length. Since larger mountain-edge cut directly affects the effective aperture of the detector, the reconstruction accuracy of the arrival direction is important to realize the background-free observation while keeping a high sensitivity. In addition, it is also very important to positively identify the neutrino shower events. The high-resolution imaging capability would be a key feature in the detection of VHE neutrinos for the first time.

6. Conclusion

In the observation of VHE neutrinos from high energy transient objects, highly precise arrival direction determination is essential to the following points: (1) Clear identification of neutrinos by distinguishing their appearance from the Earth; (2) Identification of VHE neutrino point sources. We studied the physical processes of Earth-skimming ν_τ s in detail, and found that Cherenkov τ showers of more than 1 PeV energy preserve the arrival direction of the parent ν_τ with an accuracy better than 0.1° . The Ashra detector uses newly developed light collectors which realize both a 42 degree-diameter FOV and arcminute resolution. It is capable of capturing the high-resolution images of Cherenkov emission with unprecedented precision. Based on fine imaging data, the use of maximum likelihood analysis would lead to $0.1\text{--}0.2^\circ$ accuracy in the determination of the arrival direction of Cherenkov showers even with monoscopic detection by only one light collector. The ‘‘Cherenkov τ shower ES method’’ which detects the Cherenkov photons from τ air shower has the highest point source sensitivity in the 10–100PeV range. These results indicate that the Ashra-1 detector is a unique probe of VHE neutrinos and their accelerators. The first physics results using this method were published in Ref. [26].

Acknowledgment

We thank H. Motz, S. Ogawa, P. Binder and J. Goldman for useful discussion. The Ashra-1 project is supported by the Coordination Fund for Promoting Science and Technology (157-20004100) and by Grant-in-Aid for Scientific Research (19340055, 19403004, 16403001, 23684013) from the Ministry of Education, Culture, Sports, Science and Technology in Japan.

References

- [1] E. Waxman, J. Bahcall, Phys. Rev. Lett.75 (1995) 386.
- [2] M. Vietri, ApJ453 (1995) 883.
- [3] M. Milgrom, V. Usov, ApJ449 (1995) L37.
- [4] E. Costa, et al., Nature 387 (6635) (1997) 783–785.
- [5] M. J. Rees, P. Meszaros, MNRAS 258 (1992) 41.
- [6] R. Sari, T. Piran, ApJ Lett. 455 (1995) L143.
- [7] T. Piran, Phys. Rep. 314 (1999) 575.

- [8] P. Mészáros, Rep. Prog. Phys. 69 (2006) 2259, and references therein.
- [9] N. Gehrels, et al., ApJ611 (2004) 1005.
- [10] A. A. Abdo, et al., Science 323 (2009) 1688.
- [11] M. Sasaki, Proc. of ICRR2000 Satellite Symposium: Workshop of Comprehensive Study of the High Energy Universe.
- [12] S. Barwick, Physica Scripta. T85 (2000) 106.
- [13] R. Abbasi, et al., ApJ710 (2010) 346.
- [14] R. Abbasi, et al., ApJ701 (2009) 1721.
- [15] G. Domokos, S. Kovesi-Domokos, AIP Conf. Proc. 433 (1998) 390.
- [16] A. Letessier-Selvon, AIP Conf. Proc. 566 (2000) 157.
- [17] H. Athar, G. Parente, E. Zas, Phys. Rev. D62 (2000) 093010.
- [18] D. Fargion, ApJ570 (2002) 909.
- [19] J. Feng, P. Fisher, F. Wilczek, T. Yu, Phys. Rev. Lett.88 (2002) 161102.
- [20] J. Abraham, et al., Phys. Rev. Lett.100 (2008) 211101.
- [21] S. Razzaque, P. Mészáros, E. Waxman, Phys. Rev. D69 (2004) 023001.
- [22] C. Tinney, et al., IAU Circular, 6895.
- [23] N. Mirabal, et al., GCN Circular, 4792.
- [24] M. Sasaki, J. Phys. Soc. Jpn. 77SB (Supplement B) (2008) 83.
- [25] Y. Asaoka, M. Sasaki, Nucl. Instrum. Methods Phys. Res. A 647 (2011) 34.
- [26] Y. Aita, et al., ApJ736 (2011) L12.
- [27] Y. Aita, et al., GCN Circular, 8632.
- [28] Y. Asaoka, et al., GCN Circular, 11291.
- [29] E. Wolfe, W. Wise, G. Dalrymple, U.S. Geological Survey Professional Paper 1557 (1997) 129.
- [30] T. Sjöstrand, et al., Comput. Phys. Commun. 135 (2001) 238.
- [31] S. Agostinelli, et al., Nucl. Instrum. Methods A 506 (2003) 250.
- [32] S. Iyer Dutta, et al., Phys. Rev. D63 (2001) 094020.
- [33] H. Abramowicz, A. Levy, arXiv:hep-ph/9712415v2.
- [34] B. Badelek, J. Kwiecinski, Rev. Mod. Phys. 68 (1996) 445.
- [35] S. Jadach, et al., Comput. Phys. Commun. 76 (1993) 361.
- [36] G. W. Hou, M. Huang, astro-ph/0204145.
- [37] M. Sasaki, Y. Asaoka, M. Jobashi, Astropart. Phys. 19 (2003) 37.
- [38] Y. Aita, et al., in: 31th Intl. Cosmic Ray Conf. (Lodz), ID0313, 2009.
- [39] R. Gandhi, et al., Phys. Rev. D58 (1998) 093009.
- [40] R. Gandhi, et al., Astropart. Phys. 5 (1996) 81.
- [41] J. Tseng, et al., Phys. Rev. D68 (2003) 063003.
- [42] A. M. Dziewonski, D. L. Anderson, Physics of the Earth and Planetary Interiors 25 (1981) 297.
- [43] D. Heck, et al., Report FZKA 6019.
- [44] N. Kalmykov, S. Ostapchenko, A. Pavlov, Nucl. Phys. B (Proc. Suppl.) 52B (1997) 17.
- [45] L. Anchordoqui, A. Cooper-Sarkar, D. Hooper, S. Sarkar, Phys. Rev. D74 (4) (2006) 43008.
- [46] K. Kutak, J. Kwiecinski, Eur. Phys. J. C 29 (2003) 521.
- [47] E. Henley, J. Jalilian-Marian, Phys. Rev. D73 (9) (2006) 094004.
- [48] A. Cooper-Sarkar, S. Sarkar, JHEP 01 (2008) 075.
- [49] E. Berger, et al., Phys. Rev. D77 (2008) 053007.
- [50] J. Abraham, et al., Phys. Rev. D79 (2009) 102001.
- [51] D. Kharzeev, Y. Kovchegov, K. Tuchin, Phys. Lett. B 599 (2004) 23.
- [52] K. Bartels, J. Golec-Biernat, H. Kowalski, Phys. Rev. D66 (2002) 014001.
- [53] N. Armesto, C. Merino, G. Parente, E. Zas, Phys. Rev. D77 (1) (2008) 13001.
- [54] W. Mooney, G. Laske, T. Masters, J. Geophys. Res. 103 (B1) (1998) 727–747.
- [55] C. Song, et al., Astropart. Phys. 14 (2000) 7.
- [56] T. Antoni, et al., Astropart. Phys. 14 (2001) 245.
- [57] R. Baltrusaitis, et al., Nucl. Instrum. Methods A 240 (1985) 410.
- [58] E. Zas, et al., Astropart.Phys. 1 (1993) 297.
- [59] R. Enberg, et al., Phys. Rev. D78 (2008) 043005.
- [60] A. Martin, et al., Acta Physica B 34 (2003) 3273.
- [61] H. Athar, et al., Astropart.Phys. 18 (2003) 581.